


**Extreme magnetoresistance in magnetic rare-earth monopnictides**

Linda Ye, Takehito Suzuki, Christina R. Wicker, and Joseph G. Checkelsky

*Department of Physics, Massachusetts Institute of Technology, Cambridge, Massachusetts 02139, USA* (Received 12 July 2017; revised manuscript received 17 October 2017; published 20 February 2018)

The acute sensitivity of the electrical resistance of certain systems to magnetic fields known as extreme magnetoresistance (XMR) has recently been explored in a new materials context with topological semimetals. Exemplified by  $\text{WTe}_2$  and rare-earth monopnictide  $\text{La}(\text{Sb},\text{Bi})$ , these systems tend to be nonmagnetic, nearly compensated semimetals and represent a platform for large magnetoresistance driven by intrinsic electronic structure. Here we explore electronic transport in magnetic members of the latter family of semimetals and find that XMR is strongly modulated by magnetic order. In particular,  $\text{CeSb}$  exhibits XMR in excess of  $1.6 \times 10^6\%$  at fields of 9 T whereas the magnetoresistance itself is nonmonotonic across the various magnetic phases and shows a transition from negative magnetoresistance to XMR with fields above magnetic ordering temperature  $T_N$ . The magnitude of the XMR is larger than in other rare-earth monopnictides including the nonmagnetic members and follows a nonsaturating power law to fields above 30 T. We show that the overall response can be understood as the modulation of conductivity by the Ce orbital state and for intermediate temperatures can be characterized by an effective medium model. Comparison to the orbitally quenched compound  $\text{GdBi}$  supports the correlation of XMR with the onset of magnetic ordering and compensation and highlights the unique combination of orbital inversion and type-I magnetic ordering in  $\text{CeSb}$  in determining its large response. These findings suggest a paradigm for magneto-orbital control of XMR and are relevant to the understanding of rare-earth-based correlated topological materials.

DOI: [10.1103/PhysRevB.97.081108](https://doi.org/10.1103/PhysRevB.97.081108)

Magnetoresistance (MR), i.e., the change in electrical resistance induced by application of a magnetic field, is a well-studied phenomenon in condensed-matter physics with relevance for magnetic sensing technologies and other novel electronic devices. Despite its long history, it continues to drive a rich field of study with new microscopic mechanisms and their material realizations being reported. Examples range from the classical orbital MR in metals induced by the Lorentz force [1] to linear MR in Dirac materials accompanied by quantum Landau-level formation [2]. Magnetic materials in particular host diverse MR behavior including giant magnetoresistance in magnetic multilayers [3] and colossal magnetoresistance (CMR) in oxides [4,5]. The magnitude and controllability of such effects have enabled their significant technological impact.

Towards the realization of MR capable of modifying electrical resistance on the order of the magnitude level, two strategies have seen particular success. First, materials designed on the verge of a magnetically active metal-insulator transition offer the possibility of magnetic-field control between phases capable of driving a large MR response (changes of  $\sim 10^5\%$  have been reported) [5]. Alternatively, in nonmagnetic compounds it is known that the combination of carrier compensation and high mobility can lead to nonsaturating MR not possible in single band systems [6]. The latter approach has recently seen renewed interest after the report of MR exceeding  $10^5\%$  in various topological semimetals including  $\text{WTe}_2$  [7],  $\text{PtSn}_4$  [8], and more recently  $\text{La}(\text{Sb},\text{Bi})$  [9–11]. The extremely large magnetoresistance in these systems, referred as extreme magnetoresistance (XMR), is of fundamental interest in terms of its microscopic origin and potential technological applications.

The report of XMR in rare-earth monopnictide  $\text{LaSb}$  raises the possibility of combining magnetism with high mobility semimetallic bands via replacement of La with an  $f$  electron containing rare earth element in a manner distinct from the transition-metal-based XMR materials. In the rare-earth case one may expect XMR to be preserved as the band structure and electron filling should be fundamentally unchanged whereas the magnetic degree of freedom would be enabled. Furthermore, magnetism introduced this way avoids the introduction of magnetic dopants that inevitably degrade the electronic mobility and XMR. Here we present a study of the MR of  $\text{CeSb}$  in this context. We find that this magnetic material retains the mobility required for XMR behavior and further that the magneto-orbital degree of freedom allows modulation of the appearance of XMR, leading to both negative ( $>70\%$ ) and positive ( $>1670\,000\%$ ) magnetoresistance. Comparison to the orbitally simpler  $\text{GdBi}$  demonstrates the importance of the  $f$ -orbital degree of freedom in this behavior and its role for further engineering in XMR systems.

The rare-earth monopnictides  $RX$  crystallize in the NaCl structure [Fig. 1(a)] and exhibit a rich variety of magnetic ground states [12]. In terms of electronic structure, most  $RX$  compounds are known as compensated semimetals with the conduction band deriving from rare-earth  $5d$   $t_{2g}$  states and the valence band deriving from pnictogen  $3/2p$  states, located at the  $X$  and  $\Gamma$  points in the Brillouin zone, respectively [Fig. 1(b)] [13]. Potential topological aspects of the electronic structure have recently been discussed, including Dirac semimetal nodes or topological insulating gaps along  $\Gamma$ - $X$  depending on the pnictogen [9,14] (highlighted in blue) and an unusual fourfold degenerate Dirac surface state at  $\bar{M}$  [15] (projected onto

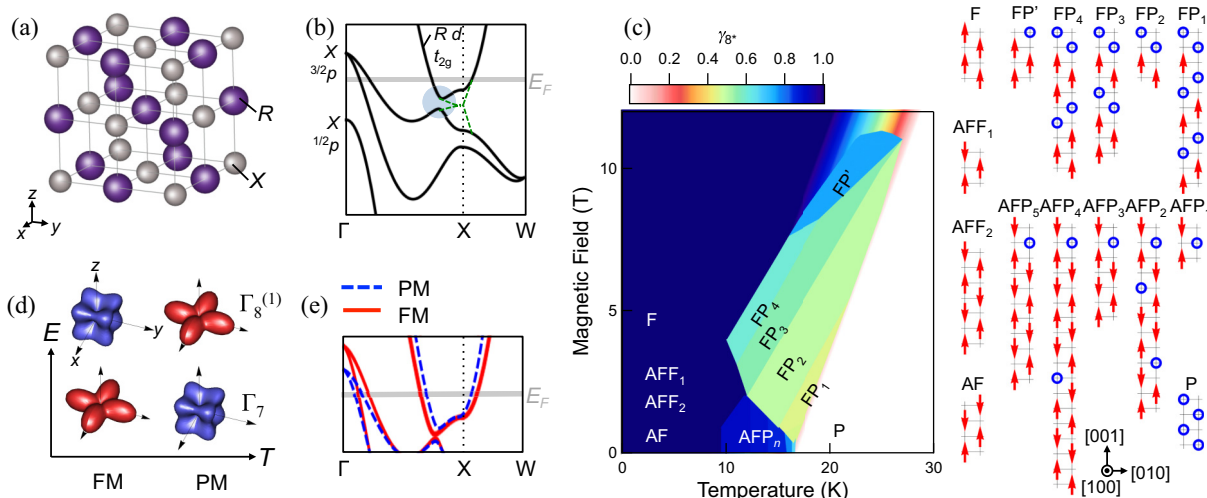


FIG. 1. (a) Rock-salt (NaCl) structure of rare-earth monopnictides  $RX$ . (b) Schematic electronic structure for  $RX$  with bands due to the pnictogen and rare-earth labeled. Topologically inverted bands (highlighted in blue) and surface bands (green) have recently been discussed. (c) Phase diagram for CeSb. The magnetic structure for the Ce layers is shown on the right, and the molar population of the magnetic  $\Gamma_{8^*}$  orbital  $\gamma_{8^*}$  is shown on the color scale. (d) Relative energies and orbital structure of the crystal-field doublets  $\Gamma_7$  and  $\Gamma_8^{(1)}$  in the (001) in-plane ferromagnetic (FM) and paramagnetic (PM) states. (e) Schematic electronic structure for CeSb in the FM and PM states.

$X$  shown in green) and are now being actively investigated [15–17]. Combining this set of electronic structure with the exchange field induced by the  $f$ -electron degree of freedom suggests  $RX$  may therefore be host to topological phases of correlated electrons [18]. This is further enriched by the reports of XMR in LaSb [9,19] and LaBi [10,11,19].

The magnetism of the  $RX$  compounds is distinct from that in simpler magnetic metals, such as Fe, Gd, and Tb and dilute magnetic semiconductors, such as  $Mn_xGa_{1-x}As$  [20] owing to the combination of strongly localized  $f$  electrons and low-density, high mobility carriers from the  $p$  and  $d$  bands. The NaCl structure enforces a significant interaction between the two with the principal pnictogen wave-function transfer being mediated through the rare-earth wave function (and vice versa) leading to a relatively wide variety of magnetic phases. This behavior is particularly distinct for the choice of a single  $f$  electron for  $R = Ce$ ; compounds CeP [21], CeAs [22], and CeSb [23] each have rich phase diagrams characterized by the mixed  $f$ -orbital occupation of Ce in the lattice.

Among the Ce monopnictides, CeSb is an unusual magnetic system, exhibiting at least 14 magnetic phases in close proximity in its magnetic field and temperature phase diagram [see Fig. 1(c)] [24]. The primary driving force for this complexity is the interplay between the semimetallic band electrons and the  $Ce^{3+} 4f^1$  states, the latter being situated near the Fermi-level  $E_F$  [25]. In the high-temperature paramagnetic phase, the preferred orbital state for the Ce ion is  $\Gamma_7$  as expected from the cubic coordination [shown schematically in Fig. 1(d)]. However, the  $\Gamma_8$  states are at an energy only 3 meV higher, and in the magnetically ordered state the cruciform  $\Gamma_8^{(1)}$  orbital becomes energetically favored. This is a result of the stronger  $p$ - $f$  hybridization effect of the  $\Gamma_8^{(1)}$  orbital (see the Supplemental Material [26]), which also leads to a shift in the electronic structure as depicted in Fig. 1(e) [25]. At intermediate  $T$  and  $B$  a complex magnetic phase diagram arises consisting of phases built by stacking paramagnetic  $\Gamma_7$

planes and ferromagnetic  $\Gamma_8^{(1)}$ -like planes as shown in Fig. 1(c). Neutron [27] and x-ray [28] scattering measurements have mapped the orbital content of these phases (the  $\Gamma_8^{(1)}$ -like planes are reported to be composed of planar orbitals that are close to a  $J_z = |\pm 5/2\rangle$  fully polarized state we hereafter refer to as  $\Gamma_{8^*}$ , see the Supplemental Material [26]); the color scale in Fig. 1(c) reflects the  $\Gamma_{8^*}$  occupation  $\gamma_{8^*}$ . Among isostructural cerium monopnictides, the phase diagram of CeSb uniquely hosts antiferromagnetic (AF), antiferroferromagnetic ( $AFF_n$ ), ferromagnetic (FM), antiferroparamagnetic ( $AFP_n$ ), ferroparamagnetic ( $FP_n$ ), and paramagnetic (PM) phases [21,29–31].

Single crystals of CeSb are grown using a Sn-flux method [32,33] from Ce (Ames Laboratory [34], 99.99%-purity), Sb (Alfa Aesar, 99.999%-purity), and Sn (Alfa Aesar, 99.995%-purity) powders. They are mixed with an atomic ratio of Ce:Sb:Sn = 1:1:20, put in an alumina crucible and sealed in a quartz tube back filled with 150 torr Ar gas. The raw materials are first heated to 1050 °C and slowly cooled to 750 °C at which point centrifuge separation of CeSb crystals from the Sn flux is performed. Single crystals of GdBi are grown using a Bi self-flux method [33] from Gd (Alfa Aesar, 99.9%-purity) and Bi (Alfa Aesar, 99.999%-purity). They are mixed with an atomic ratio of Gd:Bi = 18.5:81.5, put in an alumina crucible and sealed in a quartz tube. The raw materials are first heated to 1100 °C and slowly cooled to 950 °C followed by 4 days of annealing at which point centrifuge separation of GdBi crystals from the Bi flux is performed. In both cases subcentimeter-size rectangular crystals are obtained and oriented with single-crystal x-ray diffraction. Transport properties are measured in a commercial cryostat with a superconducting magnet. The magnetic field is applied along [001], and the current flows along [100]. Field symmetrization/antisymmetrization is performed on time-reversed field sweeps (up and down) to calculate the longitudinal/transverse resistivity and eliminate electrical pickup from contact misalignment. Magnetization is measured with a commercial superconducting quantum

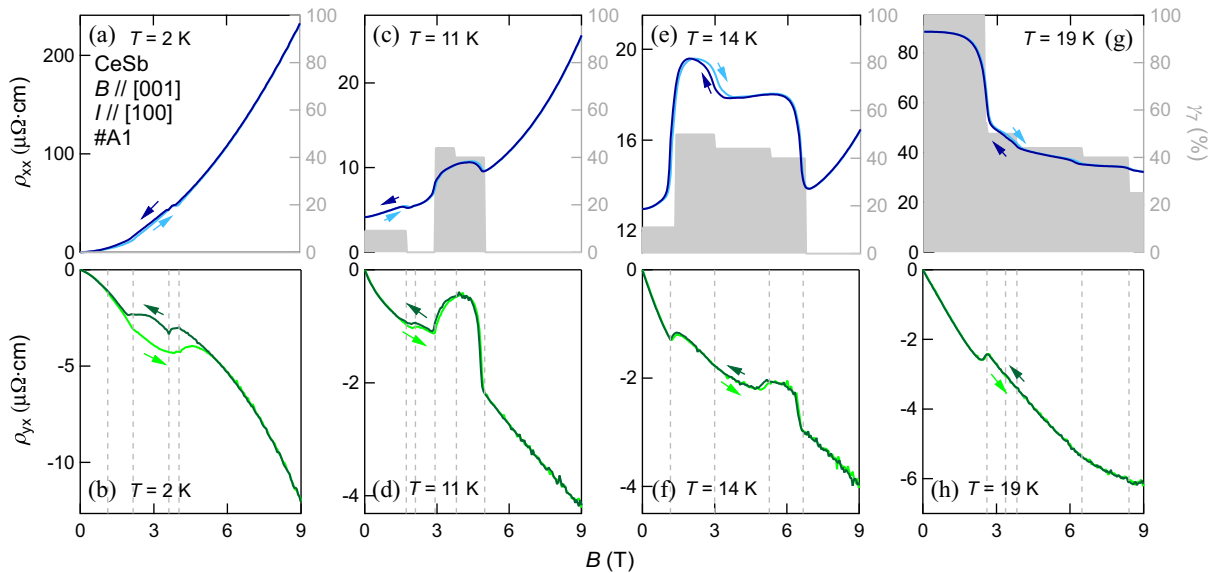


FIG. 2. (a) Longitudinal resistivity  $\rho_{xx}(B)$  for CeSb at  $T = 2$  K. Measurements with field sweeps in both directions are shown (sweep direction labeled by arrows). The right-hand axis labels the  $\Gamma_7$  orbital occupation  $\gamma_7$  expected from the magnetic structure. (b) Transverse resistivity  $\rho_{yx}(B)$  at  $T = 2$  K. Sweeps up and down are both shown (sweep direction labeled by the arrows). The vertical dashed lines mark the magnetic transitions expected on decreasing magnetic field. (c)–(h) Transport at  $T = 11, 14,$  and  $19$  K.

interference device magnetometer. Transport measurements at the National High Magnetic Field Laboratory are performed in a  $^3\text{He}$  cryostat in cell 9 with a four-probe method.

We first examine the longitudinal resistivity  $\rho_{xx}$  and transverse resistivity  $\rho_{yx}$  as a function of magnetic induction  $B$  at different characteristic temperatures  $T$  in the phase diagram. We note that  $B = \mu_0[H + (1 - N)M]$  is corrected for demagnetization effects with the demagnetization factor  $N$  calculated from the sample dimensions and magnetization  $M$  measured separately (see the Supplemental Material [26]). Starting with sample A1 at  $T = 2$  K in Fig. 2(a),  $\rho_{xx}(B)$  shows a rapid positive magnetoresistance reaching 233 500% of its zero-field value at  $B = 9$  T. This XMR behavior is comparable to that seen in  $\text{WTe}_2$  [7],  $\text{LaBi}$  [10,11], and  $\text{LaSb}$  [9], and significantly larger than that reported previously in CeSb [18,32,35–37] ( $< 50$  000%) and other magnetic RX (see the Supplemental Material, Sec. S4 [26]). Kinks in  $\rho_{xx}(B)$  are noticeable at intermediate  $B$  corresponding to the magnetic phase boundaries separating AF,  $\text{AFP}_n$ , and F states in Fig. 1(c). This is also seen in  $\rho_{yx}(B)$  shown in Fig. 2(b) where the vertical lines denote the phase boundaries observed on decreasing  $B$ . A significant hysteresis in both  $\rho_{xx}(B)$  and  $\rho_{yx}(B)$  is observed. The hysteresis is found to be sample dependent, similar to that reported in previous magnetization studies [24].

Although at  $T = 2$  K four different phases are stable at different  $B$ 's, for all  $B$ 's these phases are fully composed of  $\Gamma_8$  and thus have pure  $\Gamma_7$  layer volume fractions of  $\gamma_7 = 0\%$ . Upon increasing to  $T = 11$  K, the  $\text{AFP}_n$ ,  $\text{FP}_n$  with mixed orbital characters enter the phase diagram. Here, as shown in Fig. 2(c) the XMR response is weakened (538.5% at  $B = 9$  T), and a clear nonmonotonic behavior in  $\rho_{xx}(B)$  is observed with regions of both positive and negative  $d\rho_{xx}/dB$ . Also plotted in gray is  $\gamma_7 = 100\% - \gamma_8$ ; a correlation between intermediate regions of enhanced  $\rho_{xx}$  and  $\gamma_7$  is apparent. We expand on this below. The Hall response [Fig. 2(d)] is also sensitive

to the magnetic phase boundaries with a significant drop in magnitude in the  $\text{FP}_n$  phases where  $\gamma_7 \neq 0$ .

At higher  $T = 14$  K the same  $\Gamma_7$ -rich phases occupy a wider range of field, and significant positive magnetoresistance is observed only for  $B > 6$  T in the F state [Fig. 2(e)] with discontinuities in  $\rho_{yx}(B)$  appearing at the phase boundaries [Fig. 2(f)]. At  $T = 19$  K, above the zero-field magnetic ordering temperature  $T_N = 16$  K, positive magnetoresistance is absent up to 9 T [Fig. 2(g)], whereas at sufficient  $B$  the system transitions from the P phase to  $\text{FP}_n$  with features in  $\rho_{yx}(B)$  apparent at the critical values of  $B$  [Fig. 2(f)]. The linear Hall effect in the P phase corresponds to a single band carrier number of  $5.0 \times 10^{20}/\text{cm}^3$  or  $0.046 e^-/\text{Ce}$ . We note that the nonlinear  $\rho_{yx}(B)$  in the low-temperature F phase resembles that observed at lowest  $T$  in  $\text{LaSb}$  [19] and  $\text{LaBi}$  [11]; a multiband model must be incorporated to fully account for the behavior [38]. More broadly, at these elevated temperatures the complex evolution of  $\rho_{xx}(B)$  correlates with  $\gamma_7$ , suggestive of a connection between the orbital content and the conductivity of the system.

The evolution of the magnetoresistance is summarized in Fig. 3 where  $d\rho_{xx}/dB$  is plotted. Here the large nonsaturating magnetoresistance corresponding to XMR can be seen at low  $T$  with a superimposed Shubnikov–de Haas (SdH) oscillation. The oscillation (frequency =  $213.2 \pm 0.5$  T) corresponds to the  $k_x$ - $k_y$  cross section of the  $X_Z$  electron pocket [38]. For higher  $T > T_N$  there are regions of striking negative magnetoresistance, reaching magnitudes of  $100 \mu\Omega \text{ cm T}^{-1}$  at the phase boundary between P and FP phases. The sharp features are suppressed in transitions between  $\text{FP}_n$  phases, and an overall negative magnetoresistance is observed, reaching a magnitude of 72% at  $T = 17$  K. It is noteworthy that this negative magnetoresistance differs from conventional field suppression of magnon scattering which follows a  $B$ -linear trend and is typically at the percent level at comparable  $B$  [39].

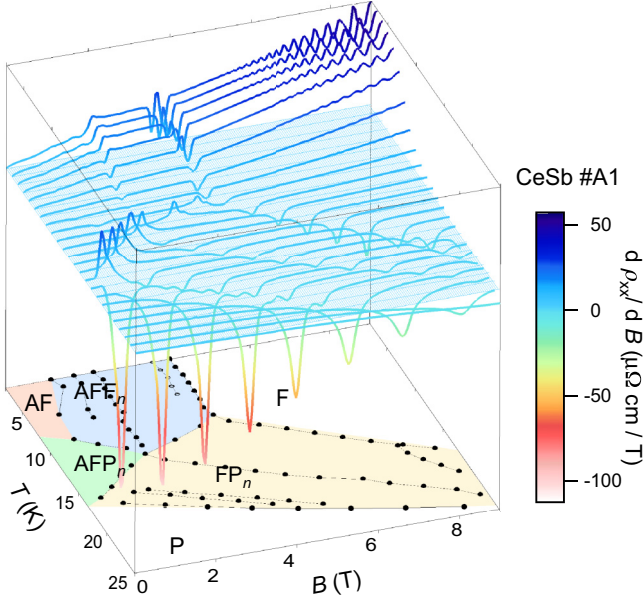


FIG. 3. Development of  $d\rho_{xx}/dB$  for field scans for different  $T$  between 2 and 25 K with decreasing  $B$ . The sharp features are projected on the  $B$ - $T$  plane and reproduce the phase diagram obtained from magnetization (the filled circles) with new features observed (the open circles).

As an aside we note that using the sharp features in  $d\rho_{xx}/dB$  it is possible to construct the phase diagram of CeSb purely from transport. This is shown projected on the  $B$ - $T$  plane in Fig. 3. The closed circles are features that reproduce those seen in  $M$  (see the Supplemental Material [26]). Interestingly, we see an additional feature that develops in the  $AFF_1$  phase in decreasing  $B$  not previously reported in magnetization studies (the open circles). This may correspond to a previously unidentified phase that further enriches the phase diagram of CeSb.

A detailed comparison of transport to the orbital content across the phase diagram is motivated by recent x-ray analysis demonstrating the evolution of the localized  $f$  wave function from  $\Gamma_{8^*}$  to  $\Gamma_7$  with increasing  $T$  across the zero-field AF,  $AFF_n$ , and P states [28]. As discussed above, compared to paramagnetic  $\Gamma_7$ ,  $\Gamma_{8^*}$  enhances hopping between the neighboring Sb sites in the plane [Fig. 1(d)] and therefore may be expected to lead to enhanced conductivity. This is qualitatively consistent with the correlation of  $\gamma_7$  and enhanced  $\rho_{xx}$  in Figs. 2(c), 2(e), and 2(g). To further quantify this, we model the system as a binary mixture with relatively low- and high-conductivity component layers composed of the  $\Gamma_7$  and  $\Gamma_{8^*}$  orbitals, respectively. A common approach to conductivity in two-component mixtures first developed for composites [40] and later applied to systems ranging from superconductors [41] to CMR manganites [42] is that of the effective medium. The underlying assumption is that a given region can be considered to be surrounded by a medium with uniform conductivity characteristic of the mixture [43]. Denoting the conductivities of  $\Gamma_7$  and  $\Gamma_{8^*}$  regions as  $\sigma_7$  and  $\sigma_{8^*}$ , respectively, in this model the total conductivity can be written as

$$\sigma_{xx}(\gamma_{8^*}) = \sigma_c + \sqrt{\sigma_c^2/4 + 8\sigma_7\sigma_{8^*}}, \quad (1)$$

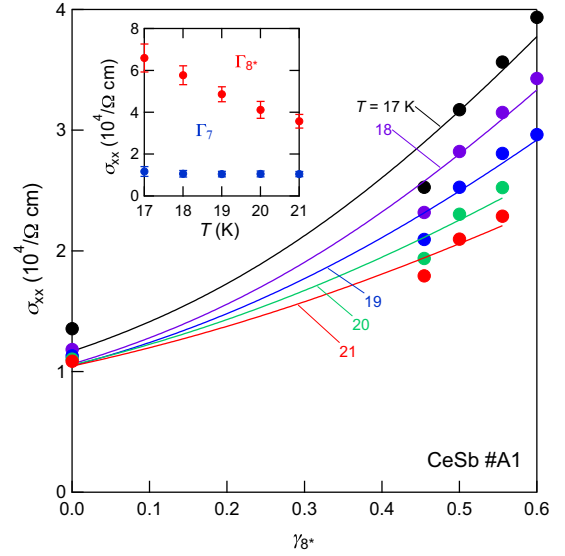


FIG. 4. Conductivity  $\sigma_{xx}$  at different  $\Gamma_{8^*}$  orbital population  $\gamma_{8^*}$  from transport results (the filled circles). The solid line at each  $T$  is a fit to an effective medium model with two components (see the text). The inset shows the  $T$  dependence of the two components of conductivity associated with the different orbital populations.

where  $\sigma_c = \sigma_7(2 - 3\gamma_{8^*}) + \sigma_{8^*}(3\gamma_{8^*} - 1)$  (see the Supplemental Material [26]). Calculating the conductivity as  $\sigma_{xx} = \rho_{xx}/(\rho_{xx}^2 + \rho_{yy}^2)$  we estimate  $\sigma_{xx}$  at each phase as its value at the central  $B$  between the phase boundaries. For simplicity we focus on the region above  $T_N$  where  $\gamma_7$  evolves most rapidly. These values are shown as a function of  $\gamma_{8^*}$  in Fig. 4 as circles with the fit to Eq. (1) as the solid line. For metal-insulator mixtures this curve takes a divergent shape reflecting the percolative transition between the two end phases [42]. Here the dependence is more gentle, suggesting components of comparable conductivity.

The orbital-dependent conductivity values found at each  $T$  are shown in the inset of Fig. 4, indicating a conductivity ratio of approximately 6 at  $T = 17$  K that diminishes on warming. Although both orbital-dependent conductivities are metallic, the ferromagnetic  $\Gamma_{8^*}$  contribution rises rapidly as  $T$  is reduced, eventually leading to the high-conductivity XMR state at low  $T$ . Whereas this confirms the above observation of enhanced resistivity in  $\Gamma_7$ -rich states, it further suggests a manner of control for XMR by the orbital degree of freedom. If the orbital content could be manipulated at low  $T$  this suggests XMR could be similarly modulated. That XMR would be absent at low  $T$  if the orbital content were modified is supported by magnetotransport reports in CeP which has a  $\Gamma_7$ -rich ground state at low  $T$  and shows negligible XMR at similar fields [44]. Application of pressure may therefore be an effective manner to tune XMR as positive pressure is known to suppress  $\Gamma_7$  in CeSb [29] and negative (chemical) pressure via La doping acts in the opposite fashion [31]. Alternatively, epitaxial thin films grown on appropriate substrates may realize materials with strain-controlled XMR.

The nonsaturating nature of the XMR in CeSb is observed with application of larger magnetic fields. As shown in Fig. 5(a), sample C1 measured up to fields above 30 T

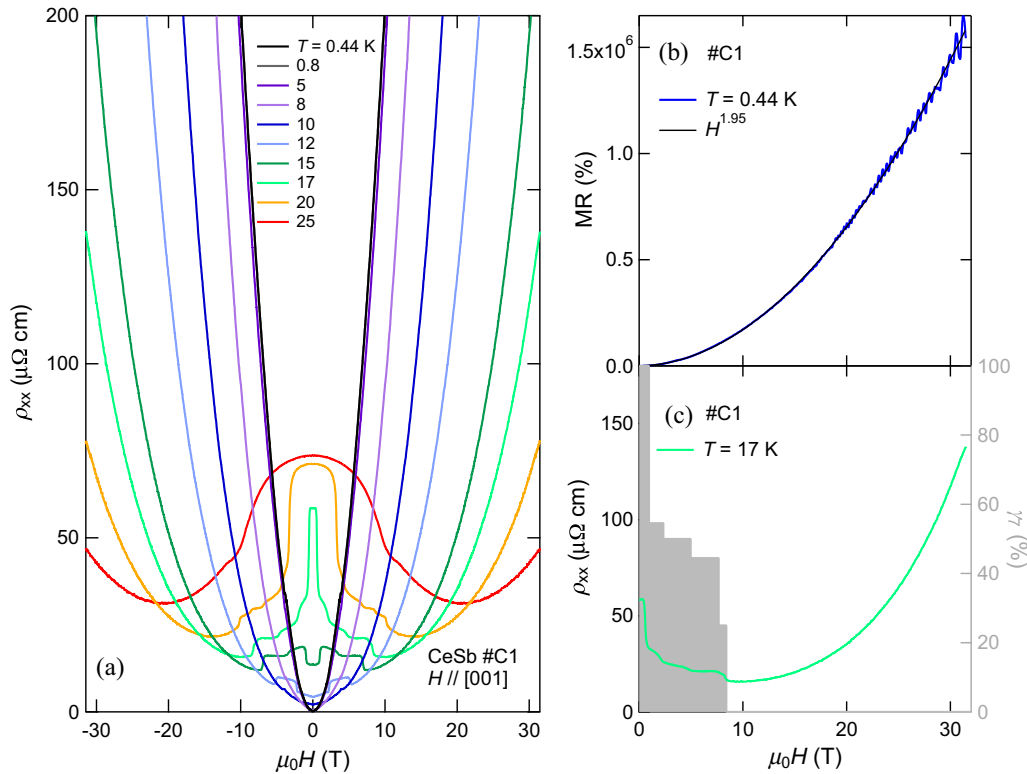


FIG. 5. (a) Magnetic-field dependence of longitudinal resistivity  $\rho_{xx}$  for CeSb sample C1 up to 31.5 T. (b) Low temperature  $T = 0.44$  K magnetotransport response fit to a 1.95 power law. (c) Intermediate temperature  $T = 17$  K magnetotransport plotted with pure  $\Gamma_7$ -layer volume fraction  $\gamma_7$ .

shows a similar crossover pattern from negative to positive magnetoresistance at intermediate  $T$  and sharply increasing XMR at the lowest  $T$ . As shown in Fig. 5(b), for  $T = 0.44$  K the MR is in excess of 1500000% at the highest fields and is well described by a 1.95 power law without sign of saturation (pronounced SdH oscillations are observed, see the Supplemental Material, Sec. S5 [26]). The large magnetic field also demonstrates the correlation of positive MR with field-induced  $\Gamma_8$ -planar orbitals [25]. For  $T = 17$  K,  $\gamma_7$  drops to zero near 9 T after which a large nonsaturating MR emerges [see Fig. 5(c)].

To further elucidate the origin of XMR at low  $T$  we compare the response of CeSb to  $RX$  compound GdBi, which is expected to be similar in electronic structure but is orbitally quenched. The overall metallicity and field response is shown in Figs. 6(a) and 6(b) for CeSb sample A1 and GdBi sample T1, respectively. For CeSb,  $\rho_{xx}$  drops dramatically below  $T_N$  reaching a value of 100 nΩ cm at  $T = 2$  K [residual resistivity ratio (RRR) = 1017], whereas application of  $B$  induces XMR. For GdBi, the behavior is similar with a drop in  $\rho_{xx}$  to 120 nΩ cm at  $T = 2$  K (RRR = 255) and XMR approximately one order of magnitude smaller at  $B = 9$  T. XMR for CeSb samples A1, B2, and B4 is shown in Fig. 6(c), the largest of which reaches 1672200% at 9 T (RRR = 2726 and residual resistivity 77 nΩ cm). This is larger than any previous report in the  $RX$  family, including the nonmagnetic LaBi and LaSb. For GdBi, XMR is observed as shown in Fig. 6(d), reaching values of 17125% (previous reports of

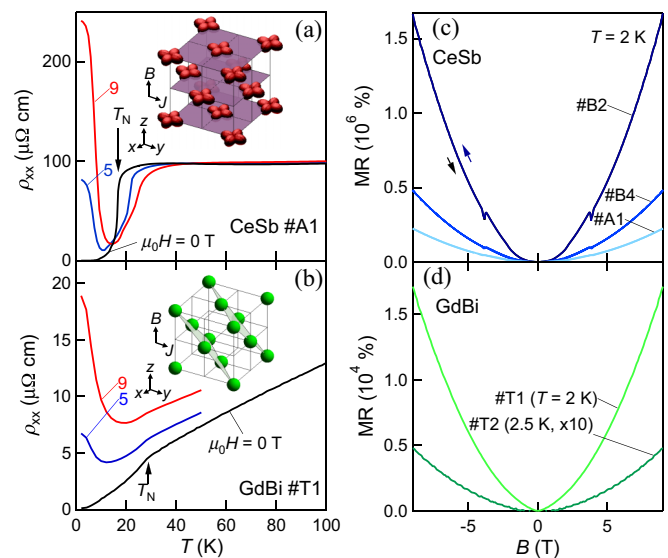


FIG. 6. (a) Temperature dependence of longitudinal resistivity  $\rho_{xx}(T)$  at different applied magnetic fields  $\mu_0 H$  for CeSb with the ordering temperature of  $T_N \approx 16$  K shown. (b)  $\rho_{xx}(T)$  at different  $\mu_0 H$  for GdBi with  $T_N \approx 28$  K labeled. The insets in (a) and (b) show the orbital shape and antiferromagnetic ordering planes with respect to the current/magnetic-field directions for the magnetic ground states of CeSb and GdBi. (c) MR defined as  $\rho_{xx}(B)/\rho_{xx}(B = 0) - 1$  at  $T = 2$  K for CeSb crystals A1, B2, and B4. (d) MR for GdBi crystals T1 and T2.

GdSb have reported similar values of 2300% [45]). Whereas for CeSb multiband fitting is complicated by the various field-induced transitions, GdBi remains in an antiferromagnetic state ( $T_N = 28$  K) up to  $B = 31$  T. In this case multiband fitting indicates a significant enhancement of mobility below  $T_N$  and nearly compensated state at the lowest  $T$  (see the Supplemental Material [26]). We therefore suggest that XMR in magnetic  $RX$  systems share a common origin with nonmagnetic  $LaX$  below  $T_N$  where magnetic scattering is suppressed. In the context of semiclassical magnetotransport, the nonsaturating power-law MR  $> 10^6\%$  for CeSb puts a strong constraint on the degree of compensation (within  $\sim 0.5\%$ ) [1], unexpected in a system with complex spin split bands. Recent analysis of XMR in YSb has shown that both exact compensation [46] and moderate compensation with mobility mismatches [47] may support this behavior whereas the power-law  $B$  dependence observed here appears to be different from the latter scenario.

The XMR in CeSb exceeds even that reported in its nonmagnetic analogs, which is unexpected from the viewpoint of the additional disorder associated with the magnetic degree of freedom. Structurally, the simple NaCl structure of  $RX$  energetically suppresses antisite disorders. Compared to other  $RX$ 's, we hypothesize that the high mobility in CeSb as a magnetic compound is rooted in the cooperative combination of the anisotropic orbital and magnetic ordering in the ground state of CeSb, enabling the large RRR and XMR behavior. In particular, the planar orbital favored in the magnetic ground state boosts the in-plane transfer integral [25], and the carriers with high in-plane mobility travel on the ferromagnetic planes defined by the type-I ordering (antiferromagnetic modulation along the [001] direction [36]) without being further scattered by a modulated magnetic potential [see the inset of Fig. 6(a)]. It is noteworthy that the planar orbital is favored in CeSb despite the preference for the  $\Gamma_7$ -orbital shape in the cubic crystal field of the NaCl structure and that an unusually large magnetic anisotropy pins the moments normal to the ordered planes [25] and strongly suppresses magnonic scattering at low  $T$ . This cooperative scenario is not the case, for example, for NdSb [37,48]. Additionally, as type-II ordering (antiferromagnetic modulation along the [111] direction [36]) is favored for  $RX$  heavier than  $EuX$  [36], we suggest that CeSb may realize a unique combination of orbital and magnetic orderings that gives rise to its high electronic mobility and large XMR in this configuration. This can be contrasted with GdBi, which shows moderate XMR here and has spherical orbitals supporting a type-II antiferromagnetism [see the inset of Fig. 6(b)]. Theoretical work may allow prediction of significant XMR in other magnetic  $RX$  and related compounds along these lines.

Finally, we note a possible connection to hydrodynamic electron transport recently discussed in nonmagnetic metals, such as PdCoO<sub>2</sub> [49]. Similar to PdCoO<sub>2</sub>, in CeSb the quantum scattering time associated with the SdH oscillations  $\tau_Q = 8.3 \times 10^{-14}$  s (Sample C1, pocket  $\alpha$ , see the Supplemental Materials [26]) is more than one order of magnitude smaller than the MR relaxation time of  $\tau_{MR} = 6.4 \times 10^{-12}$  s, indicating the dominance of momentum-conserving scattering

events over momentum-relaxing scattering events. In the case of nanostructured PdCoO<sub>2</sub>, the momentum-conserving scattering events are insufficient to relax the electron fluid to equilibrium, and it is necessary to invoke electronic viscosity associated with the physical sample boundary to account for the observed transport. In the present case of CeSb, using a Fermi velocity of  $v_F = 9 \times 10^5$  m/s of the  $\alpha_1$  pocket [15] we get a momentum-relaxing mean free path of  $l_{MR} = 5.8 \mu\text{m}$ . Although the present system size is much larger than  $l_{MR}$ , it is natural to expect that magnetic domains may be of this order given the strong easy-axis anisotropy. We propose that the domain walls may then play a role in determining the electronic viscosity in CeSb in analogy to the sample boundaries in nonmagnetic metals. The unusually high electronic mobility in CeSb may therefore allow exploration of the interplay between the magnetism and an electron fluid in the hydrodynamic regime. We note that an alternative possibility for  $\tau_{MR}/\tau_Q \gg 1$  is an internal inhomogeneity in the samples [50], which requires further study.

We have observed large nonsaturating XMR behavior in the magnetically and orbitally ordered CeSb, which exhibit the largest MR among the rare-earth monpnictide family. The presence of XMR in rare-earth monpnictides appears to be a ubiquitous phenomenon originating from their common semimetallic band structures. The use of rare-earth elements beyond La, Y, and Lu introduces correlation effects into these systems that modulate XMR. The study here demonstrates how the anomalous ordering of crystal-field states in CeSb allows this tuning with moderate  $B$  and  $T$ , exemplifying a novel principle for engineering the onset of XMR. Although electronic structure calculations in the various magnetic ground states of CeSb are challenging, it is noteworthy that previous calculations in the F state show bands with the character of type-II Weyl points in the vicinity of the Fermi level [51], indicating the possible role of topological features in these systems. Furthermore, it can be expected that magnetic order may introduce exchange effects to produce magnetically induced Weyl points for the inverted gap  $\Gamma$ - $X$  direction as have been discussed for half-Heusler systems [52,53]. Further theoretical work is needed to confirm whether such scenarios occur and to more broadly understand the underlying electronic structure in these magnetic  $RX$  systems and their potential for magneto-orbitally modified XMR.

We are grateful to L. Fu and T. Kurumaji for fruitful discussions. This research was funded, in part, by the Gordon and Betty Moore Foundation EPiQS Initiative, Grant No. GBMF3848 to J.G.C., material development by NSF Grant No. DMR-1554891, and instrumentation development with ARO Grant No. W911NF-16-1-0034. L.Y. acknowledges support by the STC Center for Integrated Quantum Materials, NSF Grant No. DMR-1231319 and by the Tsinghua Education Foundation. J.G.C. acknowledges support from the Bose Fellows Program at MIT. A portion of this Rapid Communication was performed at the National High Magnetic Field Laboratory, which is supported by National Science Foundation Cooperative Agreement No. DMR-1157490, the State of Florida, and the U.S. Department of Energy.

- [1] A. B. Pippard, *Magnetoresistance in Metals* (Cambridge University Press, New York, 1989).
- [2] A. A. Abrikosov, *Europhys. Lett.* **49**, 789 (2000).
- [3] M. N. Baibich, J. M. Broto, A. Fert, F. Nguyen Van Dau, F. Petroff, P. Etienne, G. Creuzet, A. Friederich, and J. Chazelas, *Phys. Rev. Lett.* **61**, 2472 (1988).
- [4] Y. Shapira, S. Foner, and T. B. Reed, *Phys. Rev. B* **8**, 2299 (1973).
- [5] S. Jin, M. McCormack, T. H. Tiefel, and R. Ramesh, *J. Appl. Phys.* **76**, 6929 (1994).
- [6] X. Du, S.-W. Tsai, D. L. Maslov, and A. F. Hebard, *Phys. Rev. Lett.* **94**, 166601 (2005).
- [7] M. N. Ali, J. Xiong, S. Flynn, J. Tao, Q. D. Gibson, L. M. Schoop, T. Liang, N. Haldolaarachchige, M. Hirschberger, N. P. Ong, and R. J. Cava, *Nature (London)* **514**, 205 (2014).
- [8] E. Mun, H. Ko, G. J. Miller, G. D. Samolyuk, S. L. Bud'ko, and P. C. Canfield, *Phys. Rev. B* **85**, 035135 (2012).
- [9] F. F. Tafti, Q. D. Gibson, S. K. Kushwaha, N. Haldolaarachchige, and R. J. Cava, *Nat. Phys.* **12**, 272 (2016).
- [10] F. F. Tafti, Q. D. Gibson, S. Kushwaha, J. W. Krizan, N. Haldolaarachchige, and R. J. Cava, *Proc. Natl. Acad. Sci. USA* **113**, E3475 (2016).
- [11] S. Sun, Q. Wang, P.-J. Guo, K. Liu, and H. Lei, *New J. Phys.* **18**, 082002 (2016).
- [12] F. Hulliger, in *Handbook on the Physics and Chemistry of Rare Earths*, edited by K. A. Gschneidner Jr. and L. Eyring (Elsevier B.V., Amsterdam, 1979), Vol. 4, pp. 153–236.
- [13] A. Takayama, S. Souma, T. Sato, T. Arakane, and T. Takahashi, *J. Phys. Soc. Jpn.* **78**, 073702 (2009).
- [14] M. Zeng, C. Fang, G. Chang, Y.-A. Chen, T. Hsieh, A. Bansil, H. Lin, and L. Fu, [arXiv:1504.03492](https://arxiv.org/abs/1504.03492).
- [15] N. Alidoust, A. Alexandradinata, S.-Y. Xu, I. Belopolski, S. K. Kushwaha, M. Zeng, M. Neupane, G. Bian, C. Liu, D. S. Sanchez, P. P. Shibayev, H. Zheng, L. Fu, A. Bansil, H. Lin, R. J. Cava, and M. Z. Hasan, [arXiv:1604.08571](https://arxiv.org/abs/1604.08571).
- [16] H. Oinuma, S. Souma, D. Takane, T. Nakamura, K. Nakayama, T. Mitsuhashi, K. Horiba, H. Kumigashira, M. Yoshida, A. Ochiai, T. Takahashi, and T. Sato, *Phys. Rev. B* **96**, 041120(R) (2017).
- [17] Y. Wu, Y. Lee, T. Kong, D. Mou, R. Jiang, L. Huang, S. L. Bud'ko, P. C. Canfield, and A. Kaminski, *Phys. Rev. B* **96**, 035134 (2017).
- [18] C. Guo, C. Cao, M. Smidman, F. Wu, Y. Zhang, F. Steglich, F.-C. Zhang, and H. Yuan, *npj Quantum Materials* **2**, 39 (2017).
- [19] T. Kasuya, M. Sera, Y. Okayama, and Y. Haga, *J. Phys. Soc. Jpn.* **65**, 160 (1995).
- [20] T. Dietl, *Nat. Mater.* **9**, 965 (2010).
- [21] T. Terashima, S. Uji, H. Aoki, J. A. A. J. Perenboom, Y. Haga, A. Uesawa, T. Suzuki, S. Hill, and J. S. Brooks, *Phys. Rev. B* **58**, 309 (1998).
- [22] K. Komorita, G. Kido, Y. Nakagawa, Y. S. Kwon, and T. Suzuki, *J. Magn. Magn. Mater.* **104-107**, 1241 (1992).
- [23] J. Rossat-Mignod, P. Burlet, J. Villain, H. Bartholin, W. Tcheng-Si, D. Florence, and O. Vogt, *Phys. Rev. B* **16**, 440 (1977).
- [24] O. Vogt and K. Mattenberger, *Physica B* **215**, 22 (1995).
- [25] H. Takahashi and T. Kasuya, *J. Phys. C* **18**, 2731 (1985).
- [26] See Supplemental Material at <http://link.aps.org/supplemental/10.1103/PhysRevB.97.081108> for details of crystal growth, the magnetic and orbital states of CeSb and GdBi, comparison of MR behavior among existing studies on rare earth monopnictides, quantum oscillations in CeSb, three-band fitting for GdBi, and the Kohler's scaling for CeSb and GdBi.
- [27] J. X. Boucherle, A. Delapalme, C. J. Howard, and J. Rossat-Mignod, *Physica B* **102**, 253 (1980).
- [28] K. Iwasa, A. Hannan, M. Kohgi, and T. Suzuki, *Phys. Rev. Lett.* **88**, 207201 (2002).
- [29] A. Hannan, Y. Okayama, T. Osakabe, K. Kuwahara, and M. Kohgi, *J. Phys. Soc. Jpn.* **76**, 054706 (2007).
- [30] J. Rossat-Mignod, P. Burlet, S. Quezel, J. M. Effantin, D. Delacôte, H. Bartholin, O. Vogt, and D. Ravot, *J. Magn. Magn. Mater.* **31-34**, 398 (1983).
- [31] Y. Nakanishi, T. Sakon, F. Takahashi, M. Motokawa, A. Uesawa, M. Kubota, and T. Suzuki, *Phys. Rev. B* **64**, 224402 (2001).
- [32] T. A. Wiener and P. C. Canfield, *J. Alloys Compd.* **303-304**, 505 (2000).
- [33] P. C. Canfield and Z. Fisk, *Philos. Mag. B* **65**, 1117 (1992).
- [34] Materials Preparation Center, Ames Laboratory, U.S. DOE Basic Energy Sciences, Ames, IA, USA, available at <http://www.mpc.ameslab.gov>
- [35] T. Suzuki, M. Sera, H. Shida, K. Takegahara, H. Takahashi, A. Yanase, and T. Kasuya, in *Valence Fluctuations in Solids*, edited by L. M. Falikov, W. Hanke, and M. B. Maple (North-Holland, Amsterdam, 1981), p. 255.
- [36] J. M. Fournier and E. Gratz, in *Handbook on the Physics and Chemistry of Rare Earths*, edited by K. A. Gschneidner Jr., L. Eyring, G. H. Lander, and G. R. Choppin (Elsevier B.V., Amsterdam, 1993), Vol. 17, pp. 409–537.
- [37] W. Suski and T. Palewski, in *Pnictides and Chalcogenides II (Lanthanide Monopnictides) in Landolt-Börnstein - Group III Condensed Matter*, edited by H. P. J. Wijn (Springer-Verlag, Berlin/Heidelberg, 1998), Vol. 27B1.
- [38] H. Aoki, G. W. Crabtree, W. Joss, and F. Hulliger, *J. Magn. Magn. Mater.* **97**, 169 (1991).
- [39] B. Raquet, M. Viret, E. Sondergard, O. Cespedes, and R. Mamy, *Phys. Rev. B* **66**, 024433 (2002).
- [40] R. Landauer, *J. Appl. Phys.* **23**, 779 (1952).
- [41] D. S. McLachlan, *Solid State Commun.* **69**, 925 (1989).
- [42] K. H. Kim, M. Uehara, C. Hess, P. A. Sharma, and S.-W. Cheong, *Phys. Rev. Lett.* **84**, 2961 (2000).
- [43] D. S. Machlachlan, *J. Phys. C* **20**, 865 (1987).
- [44] T. Terashima, S. Uji, H. Aoki, J. S. Qualls, J. S. Brooks, Y. Haga, A. Uesawa, and T. Suzuki, *J. Phys. Soc. Jpn.* **70**, 3683 (2001).
- [45] D. X. Li, Y. Haga, H. Shida, T. Suzuki, and Y. S. Kwon, *Phys. Rev. B* **54**, 10483 (1996).
- [46] J. Xu, N. J. Ghimire, J. S. Jiang, Z. L. Xiao, A. S. Botana, Y. L. Wang, Y. Hao, J. E. Pearson, and W. K. Kwok, *Phys. Rev. B* **96**, 075159 (2017).
- [47] J. He, C. Zhang, N. J. Ghimire, T. Liang, C. Jia, J. Jiang, S. Tang, S. Chen, Y. He, S.-K. Mo, C. C. Hwang, M. Hashimoto, D. H. Lu, B. Moritz, T. P. Devereaux, Y. L. Chen, J. F. Mitchell, and Z.-X. Shen, *Phys. Rev. Lett.* **117**, 267201 (2016).
- [48] N. Wakeham, E. D. Bauer, M. Neupane, and F. Ronning, *Phys. Rev. B* **93**, 205152 (2016).

- [49] P. J. W. Moll, P. Kushwaha, N. Nandi, B. Schmidt, and A. P. Mackenzie, *Science* **351**, 1061 (2016).
- [50] C. W. Hicks, A. S. Gibbs, A. P. Mackenzie, H. Takatsu, Y. Maeno, and E. A. Yelland, *Phys. Rev. Lett.* **109**, 116401 (2012).
- [51] Y. Kaneta, W. Iwata, T. Kasuya, and O. Sakai, *J. Phys. Soc. Jpn.* **69**, 2559 (2000).
- [52] M. Hirschberger, S. Kushwaha, Z. Wang, Q. Gibson, S. Liang, C. A. Belvin, B. A. Bernevig, R. J. Cava, and N. P. Ong, *Nat. Mater.* **15**, 1161 (2016).
- [53] T. Suzuki, R. Chisnell, A. Devarakonda, Y.-T. Liu, W. Feng, D. Xiao, J. W. Lynn, and J. G. Checkelsky, *Nat. Phys.* **12**, 1119 (2016).